How to cite: *Angew. Chem. Int. Ed.* **2024**, *63*, e202411639
doi.org/10.1002/anie.202411639

VIP Synergistic Catalysis Very Important Paper

A Planar-Structured Dinuclear Cobalt(II) Complex with Indirect Synergy for Photocatalytic CO_2-to-CO Conversion

Yun-Nan Gong[+], Si-Qi Zhao[+], Hong-Juan Wang[+], Zhao-Ming Ge, Chen Liao, Ke-Ying Tao, Di-Chang Zhong, Ken Sakai,* and Tong-Bu Lu**

Abstract: Dinuclear metal synergistic catalysis (DMSC) has been proved an effective approach to enhance catalytic efficiency in photocatalytic CO_2 reduction reaction, while it remains challenge to design dinuclear metal complexes that can show DMSC effect. The main reason is that the influence of the microenvironment around dinuclear metal centres on catalytic activity has not been well recognized and revealed. Herein, we report a dinuclear cobalt complex featuring a planar structure, which displays outstanding catalytic efficiency for photochemical CO_2-to-CO conversion. The turnover number (TON) and turnover frequency (TOF) values reach as high as 14457 and 0.40 s^{-1} respectively, 8.6 times higher than those of the corresponding mononuclear cobalt complex. Control experiments and theoretical calculations revealed that the enhanced catalytic efficiency of the dinuclear cobalt complex is due to the indirect DMSC effect between two Co^{II} ions, energetically feasible one step two-electron transfer process by $Co_2^{I,I}$ intermediate to afford $Co_2^{II,II}(CO_2^{2-})$ intermediate and fast mass transfer closely related with the planar structure.

Introduction

The massive combustion of fossil fuels and the concomitant large discharge of carbon dioxide (CO_2) into the atmosphere have caused serious energy and environmental issues.[1] Photocatalytic CO_2 reduction into high-valued chemical fuels/feedstocks has been regarded as a promising "one stone two birds" approach to the above two issues.[2] However, the activation and conversion of CO_2 molecule is difficult due to its inherent chemical inertness, which requires efficient catalysts to accomplish this process.[3] If we limit our discussion on the catalytic CO_2-to-CO conversion focused in this study, there are two important steps with high reaction energy barriers, which may determine the reactive dynamics (Scheme 1). One is the binding and reduction of CO_2 by metal center, where the linear CO_2 changes to bent CO_2 species. The other is the cleavage of the C–O bond in [O=C-OH]* intermediate. For the catalyst with single metal catalytic center, both steps occur in one

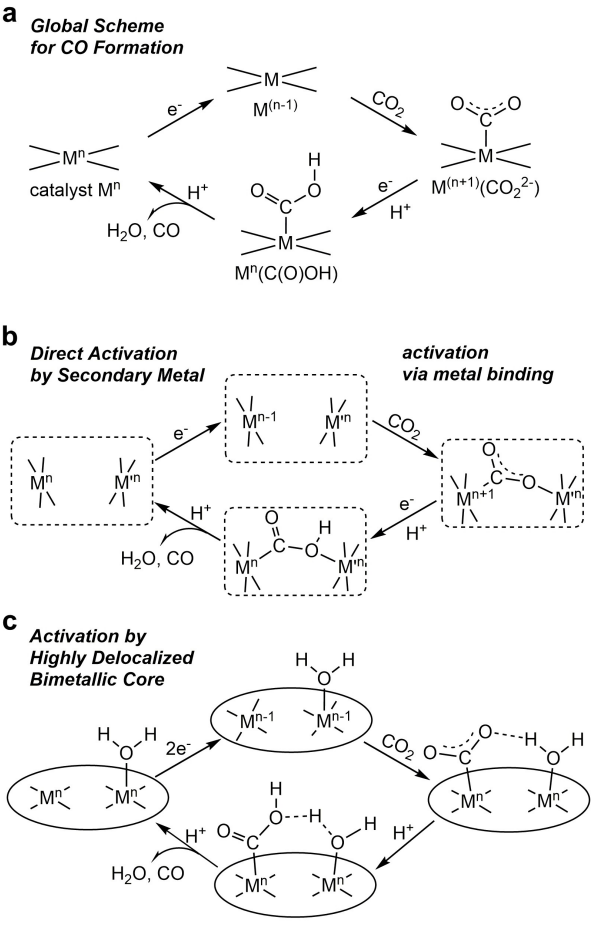

Scheme 1. Schematic representations for catalytic CO_2-to-CO reduction pathways of generalized pathways proceeding via proton-assisted, CO_2-assisted, and metal-assisted C–O cleavage (a) and direct and indirect synergistic CO_2 activation in bimetallic catalysts (b) and (c), respectively.

[*] Dr. Y.-N. Gong,[+] S.-Q. Zhao,[+] Dr. H.-J. Wang,[+] Z.-M. Ge, K.-Y. Tao, Prof. Dr. D.-C. Zhong, Prof. Dr. T.-B. Lu
MOE International Joint Laboratory of Materials Microstructure, Institute for New Energy Materials and Low Carbon Technologies, School of Materials Science and Engineering, School of Chemistry and Chemical Engineering, Tianjin University of Technology, Tianjin 300384, China
E-mail: dczhong@email.tjut.edu.cn
lutongbu@tjut.edu.cn
C. Liao, Prof. Dr. K. Sakai
Department of Chemistry, Faculty of Science, Kyushu University, Motooka 744, Nishi-ku, Fukuoka 819-0395, Japan
E-mail: ksakai@chem.kyushu-univ.jp
[+] These authors contributed equally.

active site (Scheme 1a), resulting in sluggish reaction dynamics. Therefore, over the past several years, despite a number of mononuclear transition metal complexes (e.g., Fe, Co, Ni, Cu, Mn, etc.) have been reported for photocatalytic CO_2 reduction to CO, most of them exhibit low catalytic efficiency.[4]

Based on the mechanism studies of CO_2 reduction to CO mentioned above, dinuclear metal complexes with suitable metal···metal (M···M) separations and spatial configuration will be ideal catalysts for catalyzing CO_2-to-CO conversion (Scheme 1b), as the dimetallic centers in dinuclear complexes can serve as di-active sites, not only beneficial to bind CO_2 with bridge mode, but also favorable to promote the cleavage of C–O in [O=C-OH]* intermediate, thus lowering the activation barriers of transition states and improving the catalytic efficiency of CO_2-to-CO conversion. Actually, very recently, only a few dinuclear metal complexes such as **CoCo**, **CoZn** and **CuCu** have been reported as efficient CO_2 reduction catalysts with dinuclear metal synergistic catalysis (DMSC) effect. They demonstrate enhanced catalytic activity for CO_2 reduction, in sharp contrast to the mononuclear counterpart.[5] Moreover, by regulating the metal in dual-metal sites, the catalytic activity of dinuclear complexes can be improved. For example, when one Co in dinuclear **CoCo** is replaced with Zn, the resulting **CoZn** displays significantly enhanced catalytic efficiency for CO_2-to-CO conversion compared with **CoCo**, demonstrating the strengthened DMSC effect between Co and Zn.[5d] Though many endeavors have been devoted in this field, the development of dinuclear metal complexes that can show DMSC effect remains challenge. The possible reason is that the relationship between the catalytic activity of dinuclear metal catalysts and the microenvironment around dinuclear metal centres has not been well recognized and revealed.

It is well-known that catalysts with planar molecular structures facilitate the mass transfer of substrate molecules and the release of product attached to the metal centers. In this context, the planar dinuclear metal complexes with suitable M···M separations are expected to generate DMSC effect and show high efficiency in CO_2 reduction. 2,2':6',2'':6'',2'''-quaterpyridine (qpy) and its derivatives are a type of planar organic ligands, which usually coordinate to metal centers to form planar-structured metal-quaterpyridine complexes, leaving two axial positions as active sites for binding, activating and transforming substrate molecules.[6] This feature may also benefit for the activation and conversion of CO_2. With this in mind, a dinuclear cobalt complex with a planar structure, $[Co_2L_2(H_2O)_2(NO_3)_2](NO_3)_2$ (**1**) (L = 4-amino-3,5-bis(pyridin-2-yl)-1,2,4-triazole, Figure 1a) was prepared and used as a catalyst for photocatalytic CO_2 reduction. Impressively, **1** exhibits excellent catalytic activity for the photochemical CO_2-to-CO conversion. The turnover number (TON) and turnover frequency (TOF) values reach as high as 14457 and 0.40 s^{-1} respectively, which exhibits 8.6-fold improvement than that of the corresponding mononuclear complex, $\{[CoL_2(CH_3OH)_2](C_{16}H_{33}SO_3)_2\}\cdot 1.33CH_3OH$ (**2**) (Figure 1b). Further experimental characterizations and density functional theory (DFT) calculations disclose that the enhanced

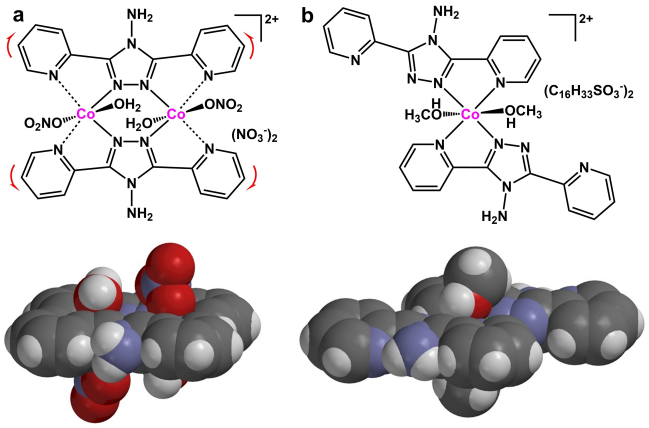

Figure 1. Chemical structures of (a) dinuclear cobalt complex **1** and (b) mononuclear complex **2**. The dashed lines for **1** denote that the Co–N(pyridyl) distances tend to distort due to the structural requirement of the ligands, as indicated by the red arrows. The space-filling models (bottom) are produced by the coordinates determined by crystallography.

catalytic efficiency of **1** is due to the indirect DMSC effect between two Co^{II} ions, that is, one Co center binds one CO_2 molecule and the other coordinates with one H_2O molecule, which can not only stabilize the adsorbed CO_2 molecule by intramolecular hydrogen bond, but also provide proton to promote the cleavage of C–O in [O=C-OH]* intermediate (Scheme 1c). Moreover, the $Co_2^{I,I}$ dimer, given by one step two-electron reduction of $Co_2^{II,II}$ dimer, can

feasibly afford the $Co_2^{II,II}(CO_2^{2-})$ intermediate to avoid the access to the more energetically demanding Co^{III} oxidation state. These features, together with the planar structure of **1**, facilitating the fast mass transfer, which significantly boost the photochemical CO_2-to-CO conversion.

Results and Discussion

1 and **2** were prepared according to the literature methods.[7] Liquid chromatography-mass spectrometry (LC–MS) of **1** shows the ion peak at *m/z* 879.0, corresponding to $\{[Co_2L_2(H_2O)_2(NO_3)_2](NO_3)_2+H^+\}^+$ ion (Figure S1). The LC–MS of **2** exhibits the ion peak at *m/z* 840.3, which can be assigned to $[CoL_2(C_{16}H_{33}SO_3)]^+$ ion (Figure S2). These LC–MS results demonstrate that **1** and **2** are dinuclear and mononuclear modes in solution, respectively, and can keep stable after dissolved in solution. Single-crystal X-ray diffraction analysis was performed to further determine the structures of **1** and **2** (Figures S3 and S4, Table S1). The results show that in **1**, each Co^{II} ion is six-coordinated by four N atoms from two L ligands in the basal plane, and two O atoms from one H_2O and one NO_3^- at the axial positions. L employs bis-bidentate coordination mode. Two L bridge two Co^{II} ions to form a dinuclear cobalt complex (Figure S3). In **2**, each Co^{II} ion is also six-coordinated by four N atoms and two O atoms. The N atoms are also from two L ligands in the basal plane, while the O atoms are from two

CH_3OH at the axial positions. Different from **1**, L in **2** adopts bidentate mode. Two L ligands coordinate with one Co^{II} ion to form a mononuclear cobalt complex (Figure S4). Further structural analyses showed that the coordination units in both **1** and **2** are approximately planar as shown by their space-filling models depicted in Figure 1, which may be beneficial for the rapidly absorbing and activating CO_2 molecules, as well as the rapid release of CO from the Co centers. Besides, the distance of Co···Co is 4.163 Å in **1** (Figure S3), which is suitable for generating DMSC effect for CO_2-to-CO conversion.

Powder X-ray diffraction (XRD) analyses revealed that the diffraction patterns of **1** and **2** are identical to the simulated ones, demonstrating that high-purity phases of **1** and **2** were obtained (Figures S5 and S6). Moreover, the temperature dependences of the magnetic susceptibility at a field of 1000 Oe (2–300 K) were also measured to clarify the spin states of **1** and **2**. At 300 K, the $\chi_M T$ values of **1** and **2** are 5.00 and 2.48 cm^3 K mol^{-1}, respectively (Figure S7).

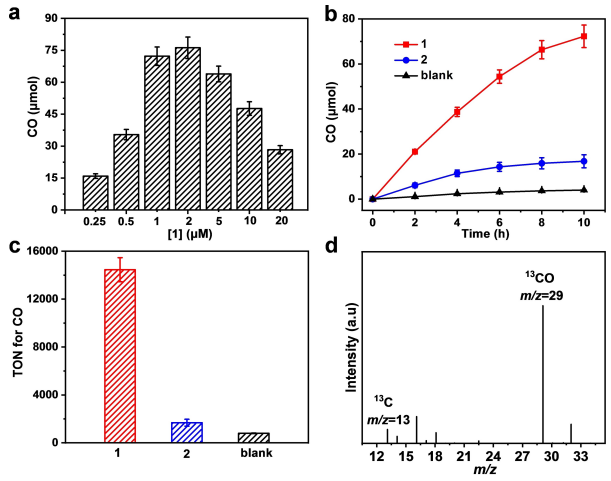

Figure 2. (a) Photocatalytic CO evolution of **1** under different concentrations (0.25–20 μM). (b) Kinetic studies of photocatalytic CO evolution by **1** (1 μM) and **2** (2 μM). (c) TON values of **1** and **2** for CO evolution. (d) Mass spectrum analysis for the gas generated from the photocatalytic CO_2 reduction by using $^{13}CO_2$ instead of $^{12}CO_2$ over **1**. Error bars are derived from standard errors from three tests.

These values are respectively larger than the values of 3.75 and 1.88 cm^3 K mol^{-1} for **1** and **2** respectively, expected for the high-spin $Co_2^{II,II}$ (S = 3/2) (**1**) and Co^{II} (S = 3/2) (**2**) by supposing an isotropic S = 3/2 spin for each metal center.[8]

Encouraged by the above structural analysis results, the photocatalytic CO_2 reduction experiments were carried out by using **1** as a catalyst, $[Ru(phen)_3](PF_6)_2$ as a photosensitizer and 1,3-dimethyl-2-phenylbenzimidazoline (BIH) as a sacrificial donor under different concentrations of **1** and light intensities. Note that the CO yield is linearly correlated to the catalyst concentration when it is less than 1 μM (Figure 2a and Table 1, Entries 1–3). At the catalyst concentrations above 1 μM, it shows a saturation followed by a gradual decrease (Figure 2a and Table 1, Entries 4–7), which was confirmed to arise from the loss of solubility of the catalyst in its PF_6^- salt above this concentration because of the presence of $[Ru(phen)_3](PF_6)_2$ (0.4 mM). Moreover, the photocatalytic activity of **1** is also closely related with the light intensity used. As shown in Table S2, with the enhancement of the light intensity, the CO yield obviously increases, while the selectivity to CO slightly decreases when it is larger than 160 mW cm^{-2}. Therefore, the optimized condition is 1.0 μM of catalyst and 160 mW cm^{-2} of light intensity. On this condition, the CO yield and selectivity by **1** reaches as high as 72.28 μmol and 95 % within 10 h respectively, corresponding to the TON and TOF values of 14457 and 0.40 s^{-1} respectively (Table 1, Entry 3; Figure 2a–2c). Under the same condition, the photocatalytic CO_2 reduction by **2** (2.0 μM) yields only 16.80 μmol of CO, with the TON and TOF values of 1680 and 0.05 s^{-1}, respectively (Table 1, Entry 8; Figure 2b, 2c). Obviously, **1** exhibits higher catalytic activity for photochemical CO_2-to-CO conversion, achieving 8.6-fold improvement over **2** quantitatively. Moreover, **1** possesses higher selectivity to CO (95 %) than **2** (89 %) (Table 1, Entries 3 and 8). These results suggest that there is a strong synergistic catalysis effect between two Co sites within **1** for photochemical CO_2-to-CO conversion.

To thoroughly investigate the photocatalytic CO_2 reduction to CO by **1**, several control experiments were carried out. As shown in Table S3, without **1**, $[Ru(phen)_3](PF_6)_2$, BIH or visible-light, negligible even no CO was detected (Entries 2–5), indicating that catalyst, photosensitizer, sacri-

Table 1: Results of photocatalytic reduction of CO_2 to CO by **1** and **2**.

Entry	Cats.	Conc. (μM)	CO [μmol]	H_2 [μmol]	$Sel._{CO}$ (%)	TON_{CO}	TOF_{CO} [s^{-1}]
1	**1**	0.25	15.92	0.83	95	12736	0.35
2	**1**	0.5	35.43	1.97	95	14172	0.39
3	**1**	1	72.28	4.02	95	14457	0.40
4	**1**	2	76.19	5.56	93	7619	0.21
5	**1**	5	63.90	7.38	90	2556	0.07
6	**1**	10	47.68	11.96	90	954	0.03
7	**1**	20	28.29	20.05	59	283	0.01
8	**2**	2	16.80	2.10	89	1680	0.05
9	**1**	1	6.10	0.47	93	1220	0.03

Conditions: $[Ru(phen)_3](PF_6)_2$ (0.4 mM), BIH (0.025 M), $CH_3CN/CH_3OH/H_2O$ ($v/v/v$ = 3:1:1), Xe lamp ($\lambda \geq 420$ nm, light intensity: 160 mW cm^{-2}), 10 h, 25 °C, under 100% CO_2 except for the Entry 9 which was performed under the gas mixture consisting of 10% CO_2 and 90% Ar. All of the experiments were performed at least three times (error below 15 %).

ficial agent, and light are all indispensable to the reduction of CO_2 to CO. When Ar was used instead of CO_2, no CO was observed (Table S3, Entry 6), indicating that the CO originates from the photocatalytic CO_2 reduction by **1**, rather than the decomposition of organic species in the photocatalytic system. This conclusion was further confirmed by isotope tracer experiment. As shown in Figure 2d, ^{13}CO signal is observed in the mass spectrum by using $^{13}CO_2$ instead of $^{12}CO_2$ in the photocatalytic system.[2g] This observation directly evidences that the generated CO comes from the reduction of CO_2.

In view of the excellent catalytic activity of **1** for photocatalytic CO_2 reduction, mixed gas containing 10 % CO_2 and 90 % Ar to simulate the flue gas (5–15 % CO_2) was used instead of 100 % CO_2, to further evaluate the catalytic performance of **1**. It was found that 6.10 μmol of CO was detected, corresponding to the TON and TOF values of 1220 and 0.03 s^{-1}, respectively (Table 1, Entry 9). Though the TON value of **1** in 10 % CO_2 decreases compared with that obtained in 100 % CO_2 (Table 1, Entry 3), this value is still higher than those of most reported catalysts behaving in 100 % CO_2 (Table S4), indicating that **1** is really highly active for photocatalytic CO_2 reduction to CO. Moreover, in such a low CO_2 concentration, **1** still exhibits a high selectivity of 93 % to CO (Table 1, Entry 9). The high activity and selectivity of **1** behaving under both 100 % and 10 % CO_2 make **1** outstanding among reported catalysts for photocatalytic CO_2 reduction (Table S4). Besides the DMSC contributing to the high activity, the free -NH_2 groups in **1** may also help to bind and reduce CO_2. To explore the proposal, we designed and synthesized the other dinuclear Co(II) complex (**3**) without -NH_2 group, which was characterized by single-crystal and powder X-ray diffraction (Figure S8). The results of photocatalytic experiment of **3** for CO_2 reduction show that the catalytic activity of **1** is 1.6-fold higher than that of **3** under the same catalytic conditions, suggesting that the free -NH_2 groups in **1** really helps to bind and reduce CO_2 (Figure S9).

Apart from the catalytic activity and selectivity, the durability of **1** in the photocatalytic CO_2 reduction was also studied. As shown in Figure S10, after 10 h of light irradiation, the production rate of CO apparently decreases, which may attribute to the degradation of **1**, $[Ru(phen)_3](PF_6)_2$ or BIH. To confirm this speculation, first of all, the UV/Vis absorption spectra of **1** and $[Ru(phen)_3](PF_6)_2$ in solution were respectively measured before and after light irradiation. The results demonstrate that the UV spectra show almost unchanged for **1** (Figure S11), while the intensity of adsorption peak significantly decreases for $[Ru(phen)_3](PF_6)_2$ after irradiation for 10 h (Figure S12), suggesting that **1** is robust during the photocatalytic process, and the deactivation of the photocatalytic CO_2 reduction system may be related with the degradation of $[Ru(phen)_3](PF_6)_2$. Then, the consecutive photocatalytic CO_2 reduction experiments were performed. After light irradiation for 10 h, a fresh equivalent of $[Ru(phen)_3](PF_6)_2$ was added in the reaction system, which can not remarkably reactivate the photocatalytic CO_2 reaction (Figure S13). However, the addition of a fresh equivalent of BIH can reactivate the ceased photocatalytic reaction with a similar rate (Figure S14). These observations suggest that the cease of the phtotocatalytic CO_2 reduction after 10 h is attributed to the consumption of BIH. Further addition of fresh BIH after 20 h, the ceased photocatalytic CO_2 reduction reaction can not be reactivated (Figure S14), implying that **1** and/or $[Ru(phen)_3](PF_6)_2$ may be degraded after 20 h. To confirm this assumption, both fresh $[Ru(phen)_3](PF_6)_2$ and fresh BIH were added in the photocatalytic reaction system after 20 h. As shown in Figure S15, the ceased photocatalytic CO_2 reduction reaction can be reactivated again, indicating that the stoppage of the photocatalytic CO_2 reduction system after 20 h is ascribed to the degradation of $[Ru(phen)_3](PF_6)_2$ and BIH. These results further illustrate that **1** is robust after photocatalysis for a period of 30 h. In addition, no nanoparticle was observed during photocatalysis, as confirmed by the dynamic light scattering (DLS) experiments. This observation, coupled with the durability results, solidly evidence that **1** possesses high robustness in photocatalytic CO_2 reduction process.

In order to well understand the DMSC effect between two Co^{II} ions in **1**, the kinetics of CO evolution by **1** was investigated in terms of both photocatalysis and electrocatalysis. The photocatalytic experiments reveal that the CO evolution rate is linear to the concentration of **1**, suggesting that the rate-determining step of catalysis is first-order in catalyst (Figure S16). The cyclic voltammogram (CV) of **1** in Ar displays a primary reduction peak at −0.94 V vs. NHE (Figure S17). On the other hand, the first reduction of **2**, corresponding to the Co^{II}/Co^{I} couple, appears at −0.95 V vs. NHE (Figure S18). As two separate one-electron transfer waves ($Co_2^{II,II}/Co_2^{II,I}$ and $Co_2^{II,I}/Co_2^{I,I}$) are not observable around this potential domain, the reduction wave of **1** at −0.94 V vs. NHE is regarded as a one-step two-electron process based on $Co_2^{II,II}/Co_2^{I,I}$ couple. This is the case in which the reduction potential for the second step ($Co_2^{II,I}/Co_2^{I,I}$) is anodically shifted with respect to that for the first step ($Co_2^{II,II}/Co_2^{II,I}$), as described elsewhere.[9] This assignment is further supported by the DFT results described below. The differential pulse voltammograms (DPVs) measured for **1** and **2** in Ar both display a single reduction peak at −0.87 and −0.88 V vs. NHE, respectively (Figure S19), consistent with the above assignments. Under CO_2 atmosphere, the CVs of both **1** and **2** exhibit much higher current densities than those observed under Ar (Figures S17 and S18). Moreover, **1** exhibits an obviously higher current density than **2** under CO_2 atmosphere, consistent with the higher photocatalytic CO_2 reduction rate of **1** compared to **2** (Figures S17 and S18). Furthermore, the current density derived from the electrocatalytic CO_2 reduction at −0.94 V linearly increases as a function of the concentration of **1** (Figure 3a and 3b), consistent with the first-order dependence of the CO evolution rate on the catalyst concentration shown by the photocatalytic experiments.

The catalytic mechanism of the photocatalytic CO_2 to CO with **1** was further revealed by fluorescence quenching experiments. As shown in Figure 3c, the maximum fluorescence emission peak of $[Ru(phen)_3]^{2+*}$ in deaerated $CH_3CN/CH_3OH/H_2O$ ($v/v/v = 3:1:1$) appears at 593 nm

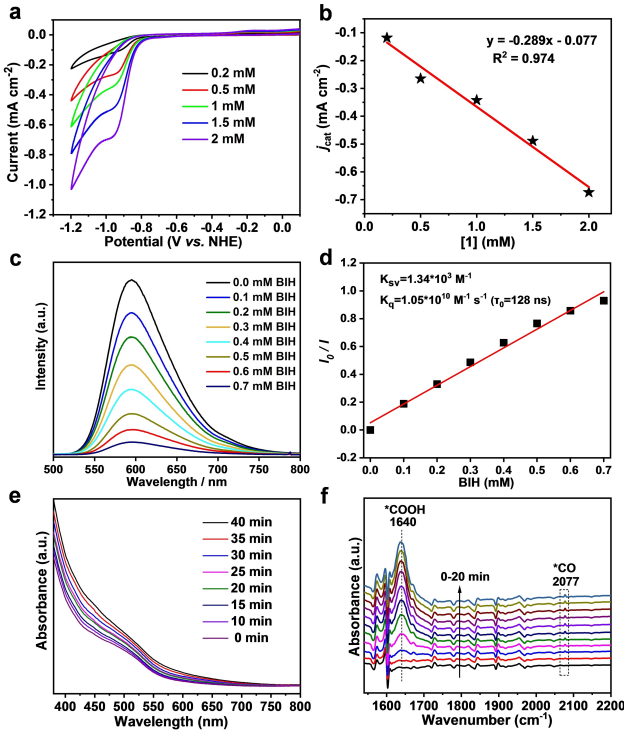

Figure 3. (a) CV curves of **1** at different concentrations. (b) Catalytic currents vs. the concentrations of **1** at −0.94 V vs. NHE. (c) Luminescence spectra of $[Ru(phen)_3](PF_6)_2$ by the addition of different concentrations of BIH. (d) Linear plots of emission intensity ratio in the absence and presence of BIH vs. the concentration of BIH. (e) UV/Vis spectra of **1** in Ar-purged $CH_3CN/CH_3OH/H_2O$ ($v/v/v = 3:1:1$) solution after electrolysis at −1.10 V vs. NHE under different times. (f) In situ FTIR spectra of **1** in photochemical CO_2-to-CO conversion.

under an excitation wavelength of 450 nm, which was gradually quenched by addition of varying concentrations of BIH. The quenching rate constant (k_q) evaluated by the Stern–Volmer plots is $1.05\times10^{10}\ M^{-1}\ s^{-1}$ (Figure 3d). In contrast, the excited state $[Ru(phen)_3]^{2+}*$ exhibits negligible fluorescence change with the addition of different concentrations of **1** (Figure S20). These results demonstrate that the quenched mode of the excited state $[Ru(phen)_3]^{2+}*$ can be assigned to an reductively quenched mechanism.[10] Thus, the reaction pathway of **1** for photocatalytic CO_2 reduction was proposed. Upon illumination, the $[Ru(phen)_3]^{2+}$ is excited firstly to produce $[Ru(phen)_3]^{2+}*$, which is quenched by BIH to form $[Ru(phen)_3]^{+}$. The oxidized $BIH^{\bullet+}$ species is easily deprotonated to form $BI^{\bullet}$, which possesses strong reducibility and can reduce $[Ru(phen)_3]^{2+}$ to $[Ru(phen)_3]^{+}$.[11] Finally, $[Ru(phen)_3]^{+}$ species transfer electrons to $Co_2^{II,II}$ of **1** to generate $Co_2^{I,I}$ intermediate, which further reduces the absorbed CO_2 to CO. To detect the reductive state of Co in **1**, UV/Vis spectroelectrochemistry investigation for **1** was conducted at −1.10 V vs. NHE. As shown in Figure 3e, it can be observed that under Ar, the intensity of adsorption peak at about 500 nm increases continuously with extension of electrolysis time, while under CO_2, the corresponding adsorption peak keeps unchanged (Figure S21). These observations suggest that the reductive state of Co (i.e., the $Co_2^{I,I}$ intermediate) was generated under Ar,[12] and the concentration of generated $Co_2^{I,I}$ intermediate gradually increases with the extension of the electrolysis time. In the presence of CO_2, the generated $Co_2^{I,I}$ intermediate are partly consumed to reduce CO_2. Thus a generation-consumption balance of $Co_2^{I,I}$ intermediate fastly build, and the UV/Vis adsorption peak at 500 nm keeps unchanged. Moreover, the photocatalytic CO_2 reduction process with **1** was in situ monitored by Fourier transform infrared spectroscopy (FTIR). As shown in Figure 3f, two new adsorption peaks at 1640 and 2077 cm^{-1}, assignable to the *COOH and *CO intermediates respectively, were detected. Their intensities gradually increase along with the increased reaction time. Both intermediates are regarded as the key intermediates during the process of CO_2 reduction to CO.[13]

In order to further elucidate the reason for the much more superior photocatalytic performance of **1** compared to **2**, possible reaction pathways for both catalysts have been predicted by the DFT calculations. As described above, the most remarkable redox property of **1**, not exhibited by **2**, is its capability of accepting two electrons at a single electrode potential based on the two-electron one-step $Co_2^{II,II}/Co_2^{I,I}$ process. As depicted in Figures 4 and S22, the first reduction step is less feasible than the second one since the second reduction potential computed is anodically shifted with respect to the first one: $E_{1,calcd} = E_{calcd}(Co_2^{II,II}/Co_2^{II,I}) = -1.21$ and $E_{2,calcd} = E_{calcd}(Co_2^{II,I}/Co_2^{I,I}) = -0.94$ V. This is the case in which the mixed-valence $Co_2^{II,I}$ intermediate is thermodynamically unstable and its disproportionation equilibrium is largely shifted to the homo-valence species, as previously described.[9] Using the DFT-computed potentials, the disproportionation constant (K_{disp}) can be computed as $K_{disp} = 3.7\times10^4$, where $E_{2,calcd} - E_{1,calcd} = (RT/F)\ln K_{disp}$, R is the gas constant, T is the absolute temperature (298.15 K), and F is the Faraday constant. It must be, however, noted that the electron transfer processes using the photochemically generated reductive equivalents (i.e., $[Ru(phen)_3]^{+}$) do not allow the two-electron one-step transfer process so that two

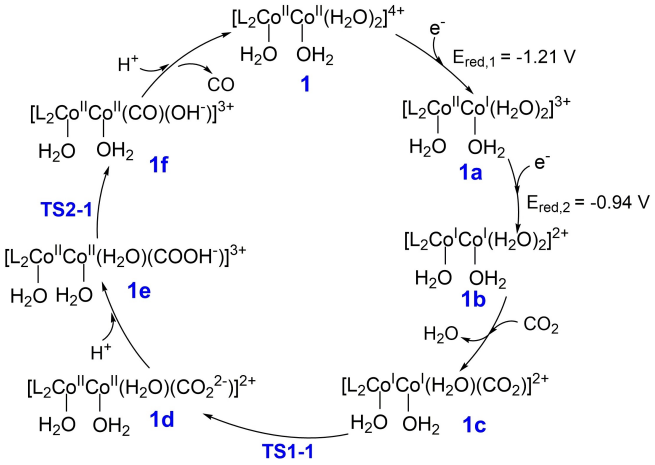

Figure 4. Proposed catalytic mechanism of **1** for reduction of CO_2 to CO through the consecutive electron transfer pathway.

consecutive one-electron transfer processes must be undertaken to afford the $Co_2^{I,I}$ intermediate (**1b**) (Figure 4). Although the formation of $Co_2^{I,I}$ intermediate via the disproportionation of the mixed-valence $Co_2^{II,I}$ species (**1a**) cannot be completely ruled out, the $[Ru(phen)_3]^{+}$-driven formation of the $Co_2^{I,I}$ species is likely to predominate due to the two order of magnitude higher concentration of the photosensitizer relative to the catalyst.

Another important feature realized by DFT is that the activation barrier for the CO_2 binding by the $Co_2^{I,I}$ intermediate is substantially low ($\Delta G^{\ddagger}=5.82$ kcal/mol for the step from **1c** to **1d** in Figures 5 and S22), clearly due to the avoidance of making access to the more thermodynamically demanding Co^{III} oxidation state. The two reductive equivalents stored in the $Co_2^{I,I}$ intermediate (**1c**) is readily utilized to afford the $Co_2^{II,II}(CO_2^{2-})$ species (**1d**) (Figure S22). In contrast, the mononuclear catalyst **2** requires the access to the Co^{III} oxidation state by promoting CO_2 binding to the one-electron reduced Co^{I} intermediate (**2b**) to yield the $Co^{III}(CO_2^{2-})$ species (**2c**) (Figures S23 and S24), as reported for various mononuclear cobalt molecular catalysts for CO_2 reduction.[10b,14] The barrier for this step is indeed rather high ($\Delta G^{\ddagger}=19.28$ kcal/mol for **2b**→**2c**), rationalizing the slower catalytic rate in CO_2 reduction by **2** (Figures 5 and S24). The highly exothermic nature of the C–O dissociation step ($Co^{III}(CO_2^{2-})+2H^{+}+e^{-} \rightarrow Co^{II}(CO)+H_2O$; Figure S23) is largely responsible for the anodically shifted reduction potential of the $Co^{III}(CO_2^{2-})/Co^{II}(COOH^{-})$ couple (−0.27 V). We may therefore conclude that the two-electron chargeable character of the dicobalt catalyst plays a significant role in its superior photocatalytic performance in CO_2-to-CO conversion.

As for the subsequent steps, the $Co_2^{II,II}(CO_2^{2-})$ intermediate (**1d**) is spontaneously stabilized by protonation to yield the $Co_2^{II,II}(COOH^{-})$ intermediate (**1e**) ($\Delta G=-11.86$ kcal/mol) (Figure S22). This intermediate further undertakes a slightly endergonic C–O cleavage ($\Delta G=1.63$ kcal/mol) by releasing OH^{-} to yield the $Co_2^{II,II}(CO)$ intermediate (**1f**) with the barrier being $\Delta G^{\ddagger}=5.03$ kcal/mol, which is only slightly lower than the barrier computed for the CO_2 binding step (5.82 kcal/mol for **1c**→**1d**) (Figure 5). Moreover, the $\Delta G^{\ddagger}$ for the cleavage of the C–O bond in [O=C-OH]* intermediate in **2** is 9.92 kcal/mol, which is significantly lower than the barrier computed for the CO_2 binding step (19.28 kcal/mol) (Figure 5). Thus, the rate-determining step (RDS) of **1** and **2** for photochemical CO_2-to-CO conversion is the CO_2 binding and reduction. Obviously, **1** exhibits lower $\Delta G^{\ddagger}$ of RDS than **2**, which strongly supports the higher catalytic performance for photochemical CO_2-to-CO conversion.

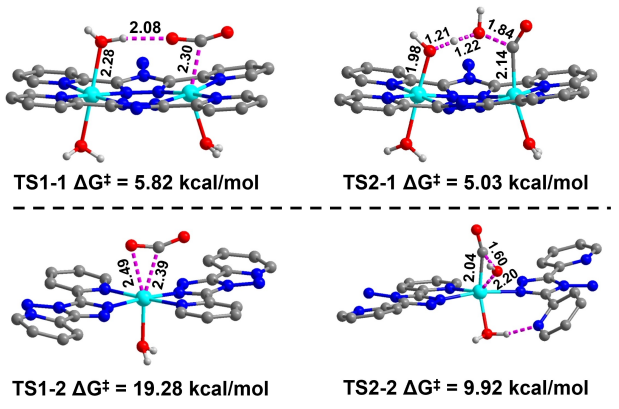

Figure 5. Free energy barriers of two transition states in CO_2 reduction to CO for **1** and **2**, the numerical values labeled on the structures represent the corresponding bond length (Å).

In addition to the rapid catalytic cycle demonstrated above for **1**, an alternative route undergoing via the CO_2 binding at the one-electron-reduced intermediate (**1a**), rather than the two-electron-reduced intermediate (**1b**), was also confirmed to be feasible as a minor, competitive CO_2 reduction pathway. As shown in Figures S25 and S26, the CO_2 binding at the $Co_2^{II,I}$ intermediate (**1c'**) may also be promoted if **1c'** encounters CO_2 rather than either $[Ru(phen)_3]^{+}$ or **1c'**, leading to afford the $Co_2^{II,III}(CO_2^{2-})$ intermediate (**1d'**). As expected from the energetic demand in making access to the Co^{III} oxidation state, the barrier for this step ($\Delta G^{\ddagger}=12.44$ kcal/mol for **1c'**→**1d'**) is much higher than that triggered by the $Co_2^{I,I}$ intermediate (5.82 kcal/mol) but still considered feasible. The subsequent step is considered to be either proton-coupled electron transfer (PCET) or reduction followed by protonation, to afford the $Co_2^{II,II}(COOH^{-})$ intermediate (**1e**) equivalent to that evolved in the major route shown in Figure S22 so that the catalytic cycle completes in the same way. The highly exothermic nature of the step affording the $Co_2^{II,II}(COOH^{-})$ intermediate also reflects the anodically shifted reduction potential for the $Co^{III}(CO_2^{2-})/Co^{II}(COOH^{-})$ couple (−0.65 V).

It's worth noting that the adjacent H_2O coordinating to one Co can form O–H···O hydrogen bond interaction with the adsorbed CO_2 in **1**, which may be beneficial for the CO_2 binding and reduction, to generate a bent CO_2^{2-} intermediate stablized by the above intramolecular hydrogen bond, thus lowering the $\Delta G^{\ddagger}$ (Figures 5 and S22).[15] To confirm this, the photochemical CO_2-to-Co conversion over **1** without H_2O coordinating to one Co was simulated. The results show that the calculated $\Delta G^{\ddagger}$ values of **TS1"-1** and **TS1"'-1** for one-step two-electron transfer and successive one-electron transfer steps are 8.73 and 16.66 kcal/mol respectively, which are much larger than that of **TS1-1** (5.82 kcal/mol) discussed above (Figure S27). These results demonstrate that the coordinated H_2O on one Co to generate indirect DMSC together with the one-step two electron transfer in **1** are thermodynamically favorable for photochemical CO_2-to-CO conversion. In addition, the results of kinetic isotope effect (KIE) of H/D reveal that the CO yields are almost unchanged when the aqueous media (H_2O) was replaced by D_2O (KIE = 1 for both catalysts **1** and **2**) (Figure S28), indicating that the proton transfer has no influence in the RDS.[16] In fact, as the RDS in photocatalytic CO_2 reduction to CO by **1** and **2** is the CO_2 binding and reduction, in which no proton participates, despite the proton takes part in the catalytic process, it has no influence on the whole photocatalytic CO_2 reduction reaction.

Additionally, some important aspects relevant to the fast catalysis by **1** can be further understood by carefully examining the electronic and structural properties of all the computed intermediates. As summarized in Tables S5 and S6, the Co–N(pyridyl) distances computed for **1** (2.243–2.264 Å) are substantially longer than those computed for the mononuclear catalyst **2** (2.181 Å), reflecting that the binucleating ligand adopted in this study is not ideal in stabilizing the bis(ligand)M_2 core (M = any metal). The instability of the mixed-valence $Co_2^{II,I}$ species is reflected in its longest average Co–N(pyridyl) distance (2.307 Å; Table S5). As illustrated in Figure S29a, 3,6-bis(pyrid-2-yl)pyridazine may provide a geometry in which the two C(pyridazine)-C(pyridyl) bond axes are linearly aligned, and thereby provides an ideal platform to stabilize a bimetallic core without giving too much structural strain in the bridging ligand geometry. In contrast, the 3,5-(pyrid-2-yl)-1,2,4-triazole ligand adopted in this work suffers from the stretching forces in all the M–N(pyridyl) bonds because of the pentacyclic character of the central ring connecting to the two pyridyl rings (Figure S29b). With this ligand, the two C(triazole)-C(pyridyl) bond axes cannot avoid having a relatively large deviation from the straight line. Such structural strains are largely suppressed in the mononuclear catalyst **2**. The same tendencies are clearly recognized in most of the catalyst intermediates. The average Co–N-(pyridyl) distance for **1** varies as follows: 2.254 (**1**), 2.307 (**1a**), 2.241(**1b**), 2.231 (**1c**), 2.283 (**1d**), 2.266 (**1e**), and 2.257 (**1f**) Å (Table S5). For **2**, it varies as follows: 2.181 (**2**), 2.140 (**2a**), 2.143 (**2b**), 2.146 (**2c**), and 2.170 (**2d**) Å (Table S6). The exceptionally long distance in **2e** (2.279 Å) is due to the strong trans influence by the OH^- ligand and is not worth discussing. It should also be notified that the Co–N(triazole) bond lengths in the catalyst intermediates derived from **1** (2.075–2.147 Å for **1**–**1f**) are quite similar to those of **2** (2.104–2.172 Å for **2**–**2d**) (Tables S5 and S6). What can be deduced from the longer coordinate bonds by the pyridyl ligands in the bimetallic catalyst is that the overall ligand field strength is much weaker in the bimetallic catalyst **1** compared to the monometallic catalyst **2**, which is consistent with the metal-based reduction potentials of **1** ($E_{1,calcd} = -1.21$ and $E_{2,calcd} = -0.94$ V) anodically shifted from that of **2** ($E_{1,calcd} = -1.40$ V). The lower electron density at the metal centers in the bimetallic catalyst can also be recognized by the longer Co–C(carbonly) distance in **1f** (2.312 Å) relative to **2e**, i.e., Co–C(carbonly) = 2.231 Å (Tables S5 and S6). In addition, both relatively long carbonyl bond lengths support the barrierless release of CO from the catalyst in the final step of catalysis. In summary, the anodically shifted metal-based reduction processes make the driving force for the electron transfer from $[Ru(phen)_3]^+$ higher in the bimetallic catalyst compared to the monometallic one, which may also contribute to the fast catalysis by **1**. Moreover, the somewhat frustrating directions of the pyridyl donors in catalyst **1** bring about the extra weakening in the donor strength, leading to the higher lability of the metal ions required for the rapid catalytic conversion processes.

On the other hand, attention should also be paid to the high-spin characters of both catalysts, which also reflect the fundamentally weak ligand field strength provided by the binucleating ligand. As shown in Figure 4 together with Figure S22, the variation in the spin density of the Co centers are shown for the whole reaction pathway in order to clarify the changes in the charge/spin density within the catalyst intermediates.[17] As shown in Figure S22, the spin densities of Co1 and Co2 are identical (2.77) in catalyst **1**, and both change into 2.53 upon one-electron reduction into **1a**, indicative of its delocalized mixed-valence $Co(1.5+)_2$ character. All the subsequent intermediates similarly possess roughly equal spin density at the two metal centers, revealing that both charge and spin are well dispersed over the bimetallic platform. Although the spin density derived from the high-spin character of each intermediate is mostly localized at the metal centers, exceptions are the CO_2^{2-}-bound species (**1d** and **2c**) in which the spin density is partially shifted to the CO_2^{2-} moiety. For instance, the spin density at the CO_2 moiety changes as follows: 0.00 (CO_2 in **1c**), −0.14 (CO_2 in **TS1-1**) and −0.28 (CO_2^{2-} in **1d**). Upon protonation of CO_2^{2-}, the spin density fully localizes at the metal centers by losing the density from the $COOH^-$ moiety (0.08 in **1e**). Similarly, the $Co^{II}(COOH^-)$ intermediate (**2d**) exhibits localized spin density at the metal center.

An important point that deserves to be mentioned again is that as the energy barrier of the CO_2 binding and reduction (5.82 kcal/mol) is slightly higher than that of the cleavage of C–O bond in [O=C-OH]* intermediate (5.03 kcal/mol), the RDS of CO_2 reduction to CO by **1** should be the former (Figure 5). Note that for reported dinuclear **CoCo** and **CoZn** based on a cryptand ligand, the RDSs are the latter.[5c,d] The difference of the RDS for CO_2 reduction to CO may be closely related with the structures of catalysts. **1** is a planar structure with one Co coordinating to a H_2O and the other Co open, which not only helps the capture of CO_2 molecule and promotes the cleavage of C–O bond in [O=C-OH]* via indirect DMSC, but also facilitates the mass transfer because of the planar structure. In contrast, **CoCo** and **CoZn** are cryptand-like structures where both active sites are confined in a cavity. The confinement of the cavity contributes to the stabilization of reaction intermediate, but conversely, this is not beneficial for the release of CO, thus affecting the mass transfer and the cleavage of C–O bond in [O=C-OH]* intermediate. As a result, at the same concentration of 1.0 μM, **1** shows an optimized TON value of 14457, much higher than those of **CoCo** (1450; Figure S30) and **CoZn** (4400).[5d] These results suggest that the planar dinuclear metal complexes are a type of ideal catalysts to boost photocatalytic CO_2-to-CO conversion, not only for the generated indirect DMSC effect, but also for the rapid mass transfer.

Conclusion

In summary, a planar-structured dinuclear cobalt complex has been successfully fabricated, which can be used as a highly efficient catalyst for the photochemical CO_2-to-CO conversion. The photocatalytic results demonstrate that this dinuclear cobalt complex exhibits remarkably higher cata-

lytic activity of 8.6 times more active than the mononuclear counterpart. The greatly enhanced catalytic efficiency can be attributed to the below characteristics: (1) the dinuclear cobalt complex shows indirect DMSC effect between two Co^{II} ions, in which one Co ion binds one CO_2 molecule and the other binds one H_2O molecule. The binding H_2O molecule, not only helps the capture of CO_2 via forming intramolecular hydrogen bond, but also promotes the cleavage of C–O in [O=C-OH]* intermediate via providing proton; (2) this dinuclear cobalt complex exhibits fast electron transfer due to the single-step two-electron redox cycling capability based on the $Co_2^{II,II}/Co_2^{I,I}$ couple, which can avoid the access to either the Co^{III} or Co^0 level while undertaking the oxidative addition of CO_2 to afford the CO_2^2-bound intermediate; (3) the planar-structure of this dinuclear cobalt complex significantly facilitates the mass transfer. This work provides new insights for researchers in designing dinuclear-metal-complex-based catalysts for synergistically photochemical CO_2-to-CO conversion.

Acknowledgements

This work was supported by National Key R&D Program of China (2022YFA1502902), the National Natural Science Foundation of China (22371208, 22271218, 22071182, 21931007), the 111 Project of China (D17003), the Natural Science Foundation of Tianjin City (23JCQNJC00570). The study was partly supported by JSPS KAKENHI grant number JP21H01952.

Conflict of Interest

The authors declare no conflict of interest.

Data Availability Statement

The data that support the findings of this study are available in the supplementary material of this article.

Keywords: dinuclear metal complex · planar structure · CO_2 reduction · dinuclear metal synergistic catalysis (DMSC) · molecular photocatalysis

[1] a) J. D. Shakun, P. U. Clark, F. He, S. A. Marcott, A. C. Mix, Z. Liu, B. Otto-Bliesner, A. Schmittner, E. Bard, *Nature* **2012**, *484*, 49–54; b) D. Shindell, C. J. Smith, *Nature* **2019**, *573*, 408–411; c) A. Goeppert, M. Czaun, J.-P. Jones, G. K. S. Prakash, G. A. Olah, *Chem. Soc. Rev.* **2014**, *43*, 7995–8048; d) F. M. Mota, D. H. Kim, *Chem. Soc. Rev.* **2019**, *48*, 205–259; e) C. L. Quéré, G. P. Peters, P. Friedlingstein, R. M. Andrew, J. G. Canadell, S. J. Davis, R. B. Jackson, M. W. Jones, *Nat. Clim. Change* **2021**, *11*, 197–199.

[2] a) J. Ran, M. Jaroniec, S.-Z. Qiao, *Adv. Mater.* **2018**, *30*, 1704649; b) L. Pan, M. Ai, C. Huang, L. Yin, X. Liu, R. Zhang, S. Wang, Z. Jiang, X. Zhang, J.-J. Zou, W. Mi, *Nat. Commun.* **2020**, *11*, 418; c) T. Kong, Y. Jiang, Y. Xiong, *Chem. Soc. Rev.* **2020**, *49*, 6579–6591; d) S. Meng, C. Chen, X. Gu, H. Wu, Q. Meng, J. Zhang, S. Chen, X. Fu, D. Liu, W. Lei, *Appl. Catal. B* **2021**, *285*, 119789; e) D. Li, M. Kassymova, X. Cai, S.-Q. Zang, H.-L. Jiang, *Coord. Chem. Rev.* **2020**, *412*, 213262; f) L.-Z. Dong, L. Zhang, J. Liu, Q. Huang, M. Lu, W.-X. Ji, Y.-Q. Lan, *Angew. Chem. Int. Ed.* **2020**, *59*, 2659–2663; g) Y.-N. Gong, W. Zhong, Y. Li, Y. Qiu, L. Zheng, J. Jiang, H.-L. Jiang, *J. Am. Chem. Soc.* **2020**, *142*, 16723–16731; h) Z. Jiang, X. Xu, Y. Ma, H. S. Cho, D. Ding, C. Wang, J. Wu, P. Oleynikov, M. Jia, J. Cheng, Y. Zhou, O. Terasaki, T. Peng, L. Zan, H. Deng, *Nature* **2020**, *586*, 549–554; i) B. Zhang, L. Sun, *Chem. Soc. Rev.* **2019**, *48*, 2216–2264; j) E. A. R. Cruz, D. Nishiori, B. L. Wadsworth, N. P. Nguyen, L. K. Hensleigh, D. Khusnutdinova, A. M. Beiler, G. F. Moore, *Chem. Rev.* **2022**, *122*, 16051–16109; k) S. Yoshino, T. Takayama, Y. Yamaguchi, A. Iwase, A. Kudo, *Acc. Chem. Res.* **2022**, *55*, 966–977.

[3] a) Y. Guo, Y. Wang, Y. Shen, Z. Cai, Z. Li, J. Liu, J. Chen, C. Xiao, H. Liu, W. Lin, C. Wang, *J. Am. Chem. Soc.* **2020**, *142*, 21493–21501; b) J. Hou, S. Cao, Y. Wu, F. Liang, Y. Sun, Z. Lin, L. Sun, *Nano Energy* **2017**, *32*, 359–366; c) W. Nie, D. E. Tarnopol, C. C. L. McCrory, *J. Am. Chem. Soc.* **2021**, *143*, 3764–3778; d) A. C. Deacy, E. Moreby, A. Phanopoulos, C. K. Williams, *J. Am. Chem. Soc.* **2020**, *142*, 19150–19160; e) B. Ma, G. Chen, C. Fave, L. Chen, R. Kuriki, K. Maeda, O. Ishitani, T.-C. Lau, J. Bonin, M. Robert, *J. Am. Chem. Soc.* **2020**, *142*, 6188–6195; f) L. Zhang, R.-H. Li, X.-X. Li, J. Liu, W. Guan, L.-Z. Dong, S.-L. Li, Y.-Q. Lan, *PNAS* **2022**, *119*, e2210550119; g) N.-Y. Huang, J.-Q. Shen, X.-W. Zhang, P.-Q. Liao, J.-P. Zhang, X.-M. Chen, *J. Am. Chem. Soc.* **2022**, *144*, 8676–8682; h) W. Lin, J. Lin, X. Zhang, L. Zhang, R. A. Borse, Y. Wang, *J. Am. Chem. Soc.* **2023**, *145*, 18141–18147.

[4] a) J.-W. Wang, W.-J. Liu, D.-C. Zhong, T.-B. Lu, *Coord. Chem. Rev.* **2019**, *378*, 237–261; b) N. Elgrishi, M. B. Chambers, X. Wang, M. Fontecave, *Chem. Soc. Rev.* **2017**, *46*, 761–796; c) P. B. Pati, R. Wang, E. Boutin, S. Diring, S. Jobic, N. Barreau, F. Odobel, M. Robert, *Nat. Commun.* **2020**, *11*, 3499; d) Y. Yao, Y. Gao, L. Ye, H. Chen, L. Sun, *J. Energy Chem.* **2018**, *27*, 502–506; e) D.-C. Liu, H.-J. Wang, T. Ouyang, J.-W. Wang, L. Jiang, D.-C. Zhong, T.-B. Lu, *ACS Appl. Energ. Mater.* **2018**, *1*, 2452–2459; f) X. Zhang, M. Cibian, A. Call, K. Yamauchi, K. Sakai, *ACS Catal.* **2019**, *9*, 11263–11273; g) F.-Y. Ren, K. Chen, L.-Q. Qiu, J.-M. Chen, D. J. Darensbourg, L.-N. He, *Angew. Chem. Int. Ed.* **2022**, *61*, e202200751; *Angew. Chem.* **2022**, *134*, e202200751; h) B. Ma, M. Blanco, L. Calvillo, L. Chen, G. Chen, T.-C. Lau, G. Drazic, J. Bonin, M. Robert, G. Granozzi, *J. Am. Chem. Soc.* **2021**, *143*, 8414–8425; i) D. Liu, H. Ma, C. Zhu, F. Qiu, W. Yu, L.-L. Ma, X.-W. Wei, Y.-F. Han, G. Yuan, *J. Am. Chem. Soc.* **2024**, *146*, 2275–2285.

[5] a) Z. Guo, G. Chen, C. Cometto, B. Ma, H. Zhao, T. Groizard, L. Chen, H. Fan, W.-L. Man, S.-M. Yiu, K.-C. Lau, T.-C. Lau, M. Robert, *Nat. Catal.* **2019**, *2*, 801–808; b) L.-M. Cao, H.-H. Huang, J.-W. Wang, D.-C. Zhong, T.-B. Lu, *Green Chem.* **2018**, *20*, 798–803; c) T. Ouyang, H.-H. Huang, J.-W. Wang, D.-C. Zhong, T.-B. Lu, *Angew. Chem. Int. Ed.* **2017**, *56*, 738–743; d) T. Ouyang, H.-J. Wang, H.-H. Huang, J.-W. Wang, S. Guo, W.-J. Liu, D.-C. Zhong, T.-B. Lu, *Angew. Chem. Int. Ed.* **2018**, *57*, 16480–16485; e) J. Bharti, L. Chen, Z. Guo, L. Cheng, J. Wellauer, O. S. Wenger, N. Wolff, K.-C. Lau, T.-C. Lau, G. Chen, M. Robert, *J. Am. Chem. Soc.* **2023**, *145*, 25195–25202.

[6] a) L. Chen, G. Chen, C.-F. Leung, C. Cometto, M. Robert, T.-C. Lau, *Chem. Soc. Rev.* **2020**, *49*, 7271–7283; b) Z. Guo, S. Cheng, C. Cometto, E. Anxolabéhère-Mallart, S.-M. Ng, C.-C. Ko, G. Liu, L. Chen, M. Robert, T.-C. Lau, *J. Am. Chem. Soc.* **2016**, *138*, 9413–9416; c) L. Frayne, N. Das, A. Paul, S. Amirjalayer, W. J. Buma, S. Woutersen, C. Long, J. G. Vos, M. T. Pryce, *ChemPhotoChem* **2018**, *2*, 323–331.

[7] a) J. Qin, N. Lei, H.-L. Zhu, *J. Coord. Chem.* **2014**, *67*, 1279–1289; b) N. G. White, H. L. C. Feltham, C. Gandolfi, M. Albrecht, S. Brooker, *Dalton Trans.* **2010**, *39*, 3751–3758.
[8] a) S. Fortier, J. J. L. Roy, C.-H. Chen, V. Vieru, M. Murugesu, L. F. Chibotaru, D. J. Mindiola, K. G. Caulton, *J. Am. Chem. Soc.* **2013**, *135*, 14670–14678; b) L. Chen, J. Wang, J.-M. Wei, W. Wernsdorfer, X.-T. Chen, Y.-Q. Zhang, Y. Song, Z.-L. Xue, *J. Am. Chem. Soc.* **2014**, *136*, 12213–12216.
[9] a) R. L. Myers, I. Shain, *Anal. Chem.* **1969**, *41*, 980; b) D. E. Richardson, H. Taube, *Inorg. Chem.* **1981**, *20*, 1285–1287.
[10] a) B. Han, X. Ou, Z. Deng, Y. Song, C. Tian, H. Deng, Y.-J. Xu, Z. Lin, *Angew. Chem. Int. Ed.* **2018**, *57*, 16811–16815; b) A. Call, M. Cibian, K. Yamamoto, T. Nakazono, K. Yamauchi, K. Sakai, *ACS Catal.* **2019**, *9*, 4867–4874.
[11] D. Hong, T. Kawanishi, Y. Tsukakoshi, H. Kotani, T. Ishizuka, T. Kojima, *J. Am. Chem. Soc.* **2019**, *141*, 20309–20317.
[12] a) L. Francàs, S. Corby, S. Selim, D. Lee, C. A. Mesa, R. G. Ernest Pastor, I. E. L. Stephens, K.-S. Choi, J. R. Durrant, *Nat. Commun.* **2019**, *10*, 5208; b) P. Ghosh, S. deVos, M. Lutz, F. Gloaguen, P. Schollhammer, M.-E. Moret, R. J. M. K. Gebbink, *Chem. Eur. J.* **2020**, *26*, 12560–12569.
[13] a) X. Li, Y. Sun, J. Xu, Y. Shao, J. Wu, X. Xu, Y. Pan, H. Ju, J. Zhu, Y. Xie, *Nat. Energy* **2019**, *4*, 690–699; b) Y. Li, B. Wei, M. Zhu, J. Chen, Q. Jiang, B. Yang, Y. Hou, L. Lei, Z. Li, R. Zhang, Y. Lu, *Adv. Mater.* **2021**, 2102212.
[14] a) Y. Sakaguchi, A. Call, K. Yamauchi, K. Sakai, *Dalton Trans.* **2021**, *50*, 15983–15995; b) X. Zhang, K. Yamauchi, K. Sakai, *ACS Catal.* **2021**, *11*, 10436–10449.
[15] P. Gotico, L. Roupnel, R. Guillot, M. Sircoglou, W. Leibl, Z. Halime, A. Aukauloo, *Angew. Chem. Int. Ed.* **2020**, *59*, 22451–22455; *Angew. Chem.* **2020**, *132*, 22637–22641.
[16] a) W. Ma, S. Xie, T. Liu, Q. Fan, J. Ye, F. Sun, Z. Jiang, Q. Zhang, J. Cheng, Y. Wang, *Nat. Catal.* **2020**, *3*, 478–487; b) W. Ma, S. Xie, X.-G. Zhang, F. Sun, J. Kang, Z.g Jiang, Q. Zhang, D.-Y. Wu, Y. Wang, *Nat. Commun.* **2019**, *10*, 892.
[17] a) J. Lan, T. Liao, T. Zhang, L. W. Chung, *Inorg. Chem.* **2017**, *56*, 6809–6819; b) J. Wang, F.-Q. Bai, B.-H. Xia, L. Feng, H.-X. Zhang, Q.-J. Pan, *Phys. Chem. Chem. Phys.* **2011**, *13*, 2206–2213.

Manuscript received: June 20, 2024
Accepted manuscript online: July 8, 2024
Version of record online: August 23, 2024